# Prominent Reducing Gas-Sensing Performances of n-SnO$_2$ Nanowires by Local Creation of $p{-}n$ Heterojunctions by Functionalization with p-Cr$_2$O$_3$ Nanoparticles

Sun-Woo Choi, Akash Katoch, Jae-Hun Kim, and Sang Sub Kim*

Department of Materials Science and Engineering, Inha University, Incheon 402-751, Republic of Korea

S *Supporting Information*

ABSTRACT: A novel approach to improving the reducing gas-sensing properties of n-type nanowires (NWs), by locally creating $p{-}n$ heterojunctions with p-type nanoparticles (NPs), is proposed. As a model system, this work investigates the sensing behaviors of n-SnO$_2$ NWs functionalized with p-Cr$_2$O$_3$ NPs. Herein, n-SnO$_2$ NWs demonstrate greatly improved reducing gas-sensing performance when functionalized with p-Cr$_2$O$_3$ NPs. Conversely, such functionalization deteriorates the oxidizing gas-sensing properties of n-SnO$_2$ NWs. These phenomena are closely related to the local suppression of the conduction channel of n-type NWs, in the radial direction, beneath the $p{-}n$ heterojunction by the flow of charge carriers. The approach used in this work can be used to fabricate sensitive reducing-gas sensors based on n-type NWs.
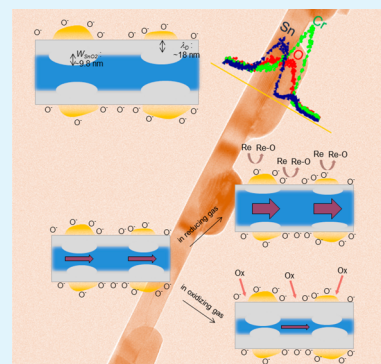
KEYWORDS: gas sensor, sensing mechanism, SnO$_2$ nanowire, Cr$_2$O$_3$ nanoparticle, electronic sensitization

1. INTRODUCTION

Thanks to their high sensor responses, reliabilities, and reproducibilities, high quality metal oxide semiconductor (MOS) nanowires (NWs) with large surface-to-volume ratios have recently received a lot of attention for use as chemical gas sensors.[1−5] Despite the promising potential of MOS NWs for gas sensor applications, some aspects such as improvement of gas responses, low selectivities, and high working temperatures are persistent challenges to their actual implementation.[6] Accordingly, various strategies have been suggested for the enhancement of their gas-sensing abilities and lowering the power consumption of NWs sensors.[7−22] These strategies include, for instance, doping with noble metals,[7,8] surface functionalization,[9−11] core−shell structures,[13−15] and the use of specially designed nanostructured materials.[16−22] In addition, formation of oxide nanoparticle (NP)−NW heterojunctions was used to improve NWs' sensing performances.[23−25] Molecule-based chemical vapor growth of aligned oxide NWs was also used as a sensor platform.[26] Despite considerable progress in improving gas-sensing capabilities of NWs, modification of NW conduction channels has rarely been attempted.

Recently, we reported the preparation of metallic-Ag/p-Ag$_2$O NP-functionalized SnO$_2$ microrods.[27] The microrods exhibited significantly improved sensing for oxidizing gases, including NO$_2$, because their conduction channels were greatly expanded by the electron transfer from the NPs to the microrods. In another report,[28] semiconductor NWs modified with organic self-assembled monolayers were proposed for the selective detection of a single gas species. More recently, we synthesized

CuO−ZnO core−shell nanofibers[29] that showed sensitive and selective detection of reducing gases. Radial modulation of the conduction channel, caused by electron transfer from the ZnO shell layer to the CuO core fiber, was found to be critical to gas-sensing performance. All these results clearly suggest that suppression/expansion of NW conduction channels by charge carrier flow between locally surface-attached materials and NWs can effectively achieve enhanced detection of oxidizing or reducing gases.

As an extension of the above-mentioned results[27,29] we report, for the first time, n-SnO$_2$ NWs that demonstrate the prominent improvement of detection capability for reducing gases by attachment of p-Cr$_2$O$_3$ NPs. Electron transfer from n-SnO$_2$ NWs to p-Cr$_2$O$_3$ NPs at the $p{-}n$ interfaces results in local suppression of the conduction channels of the n-SnO$_2$ NWs. In this case, exposure to reducing gases increases conduction channel modulation along NW radial direction more than exposure to oxidizing gases. The local creation of $p{-}n$ heterojunctions can be a novel approach to improving sensing performances of n-type NWs for reducing gases.

2. EXPERIMENTAL SECTION

Growth of n-SnO$_2$ NWs. SnO$_2$ NWs were grown by the well-known vapor−liquid−solid (VLS) method. Patterned-interdigital electrodes (PIEs) were made on SiO$_2$-grown Si (100) substrates by conventional photolithography. The details of the fabricated PIEs are

as follows: The total number of electrode pads was 20; each electrode pad was 1.05 mm long and 20 μm wide; the gap between the neighboring electrode pads was 10 μm. A trilayer Au (3 nm)/Pt (200 nm)/Ti (50 nm) electrode, produced by the sequential sputtering method, was used. The Au top layer acted as a catalyst layer for the VLS growth of SnO_2 NWs, which facilitated the formation of a SnO_2 NW network between neighboring catalytic-layer pads. We have described the experimental conditions used to synthesize such SnO_2 NW networks in detail in a previous report.[30]

Functionalization of p-Cr_2O_3 NPs. To functionalize p-Cr_2O_3 NPs on SnO_2 NWs, A Cr film of thickness ~20 nm was first deposited on the SnO_2 NWs by sputtering a Cr target. The sputtering conditions were as follows: 2 in. diameter, 0.25 in. thick pure Cr target; target-to-substrate distance of 10 cm; input power of 100 W; chamber atmosphere of 10 mTorr Ar; deposition carried out for 30 s. The Cr-deposited SnO_2 NWs were subsequently annealed at 700 °C for 2 h in air, creating discontinuous p-Cr_2O_3 NPs on the n-SnO_2 NWs.

Microstructure Observation. X-ray diffraction (XRD, Philips X'pert MRD diffractometer) with a Cu Kα ($\lambda = 1.54$ Å) radiation source was used to investigate the phases and crystalline structures of samples. Field-emission scanning electron microscopy (FE-SEM, Hitachi S-4200) and transmission electron microscopy (TEM, Philips CM-200) were employed to examine microstructures. The TEM instrument was equipped with an energy-dispersive spectroscopy (EDS) analyzer, which was used to obtain compositional information.

Sensing Measurement. The sensing performances of the p-Cr_2O_3 NPs-functionalized n-SnO_2 NWs were investigated not only for various oxidizing gases, such as NO_2, O_2, and SO_2 but also for various reducing gases, such as H_2, CO, C_6H_6, and C_7H_8, using a gas sensing system. The sensors were placed in a horizontal-type tube furnace and the measuring temperature was varied between 200 and 400 °C. Gas concentrations were controlled by changing the mixing ratios of dry air-balanced target gases to dry air using accurate mass flow controllers. According to the specifications provided by the gas manufacturer, the content of water vapor in the dry air was less than 3 ppm, indicating that the humidity effect can be negligible. Gas response (R) was evaluated as the ratio of R_g/R_a (or R_a/R_g), where R_a is the resistance in the absence of a target gas and R_g is the resistance measured in the presence of a target gas for oxidizing gases (or for reducing gases).

3. RESULTS AND DISCUSSION

The microstructures of single crystalline n-SnO_2 NWs grown on the PIEs-patterned SiO_2/Si substrates by VLS are shown in Figure 1. A schematic representing a feature of the networked n-SnO_2 NWs is shown in Figure 1a. A plane-view FE-SEM image taken of part of a SnO_2 NW on a PIE network is shown in Figure 1b. It is clear that SnO_2 NWs were selectively grown on the PIE catalytic pads (pad width and gap were 20 and 10 μm, respectively) and that a network of SnO_2 NWs between adjacent pads developed. A cross sectional FE-SEM image, shown in Figure 1c, more clearly demonstrates the nature of the network. Figure 1d shows a region of the n-SnO_2 NW network. Diameters of the SnO_2 NWs ranged from 50 to 80 nm, and their lengths were several tens of micrometers. Further microstructural analysis was done by TEM. Figure 1e shows a low-magnification TEM image of an individual SnO_2 NW, revealing its high crystalline quality and no evidence of significant structural defects, such as dislocations or stacking faults. The selected area electron diffraction pattern, shown in the inset of Figure 1e, obtained from a region of the SnO_2 NW, shows sharp diffraction spots, again confirming single crystallinity. The high-resolution lattice image, shown in Figure 1f, reveals the (200) fringes with a distance 0.47 nm. The growth direction of the NW is indicated as the arrow in the figure.
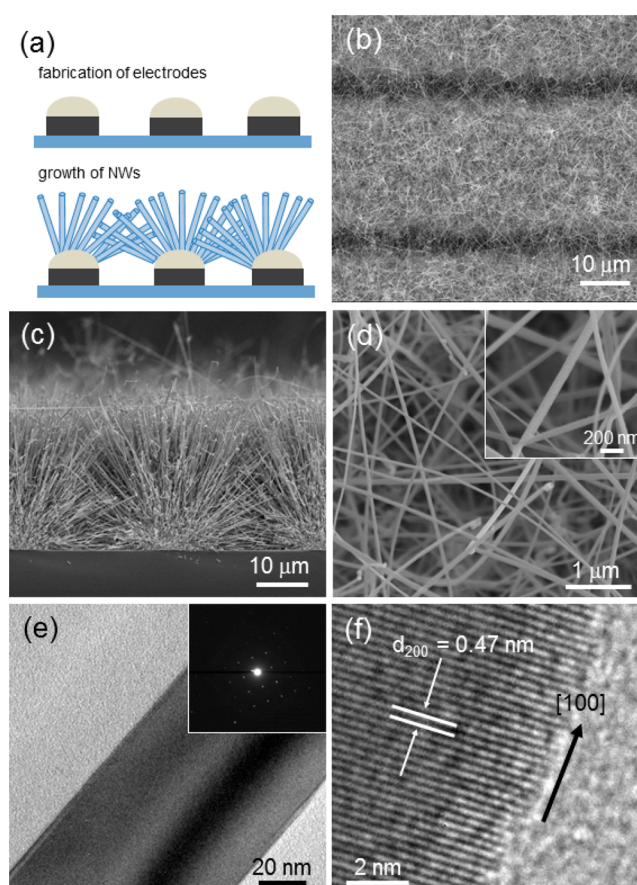

Figure 1. (a) Schematic showing the procedure used for the fabrication of electrode layers and the growth of n-SnO_2 NW networks by VLS. Microstructures of n-SnO_2 NW networks: (b) plane-view image, (c) cross-section image, and (d) FE-SEM image of a network region. (e) Low-magnification TEM image of an individual SnO_2 nanowire. The inset presents a selected area electron diffraction pattern. (f) High-resolution TEM image showing the lattice fringes.

p-Cr_2O_3 NPs were functionalized on these n-SnO_2 NW networks by the sputtering and subsequent heat treatment method. An overall plane-view image of the microstructure of p-Cr_2O_3 NPs-functionalized n-SnO_2 NWs is shown in Figure 2a. Figure 2b,c shows low- and high-magnification FE-SEM images, respectively, revealing that NPs were uniformly attached to the surfaces of the nanowires. Elongated-shape NPs on the surface of a SnO_2 nanowire, observed by TEM, are shown in Figure 2d. These island-shape NPs are identified as Cr_2O_3 in the high-resolution TEM image shown in Figure 2e. Lattice fringes, not only from the SnO_2 NW but also from the Cr_2O_3 NP, are clearly shown. The interplanar spacing, ~2.48 Å corresponds to the previously reported d_{110} spacing of Cr_2O_3.[31] It is of note that the interface between SnO_2 and Cr_2O_3 appears clearly, without considerable interdiffusion, which is suggestive of an abrupt p-Cr_2O_3/n-SnO_2 p–n heterojunction interface. As shown in Figure 2f, EDS elemental mapping profiles of Sn, Cr, and O again confirm the composition of the NPs to be Cr_2O_3. The profile for Cr is localized within the NP.

Cr_2O_3, with a corundum structure, and tetragonal, rutile SnO_2 phases were found to coexist in p-Cr_2O_3 NPs-functionalized n-SnO_2 NWs, as shown in the typical XRD pattern presented in Figure S1 of the Supporting Information. All recognizable reflection peaks can be indexed to tetragonal, rutile SnO_2 (JCPDS No. 88-0287) and corundum Cr_2O_3 with
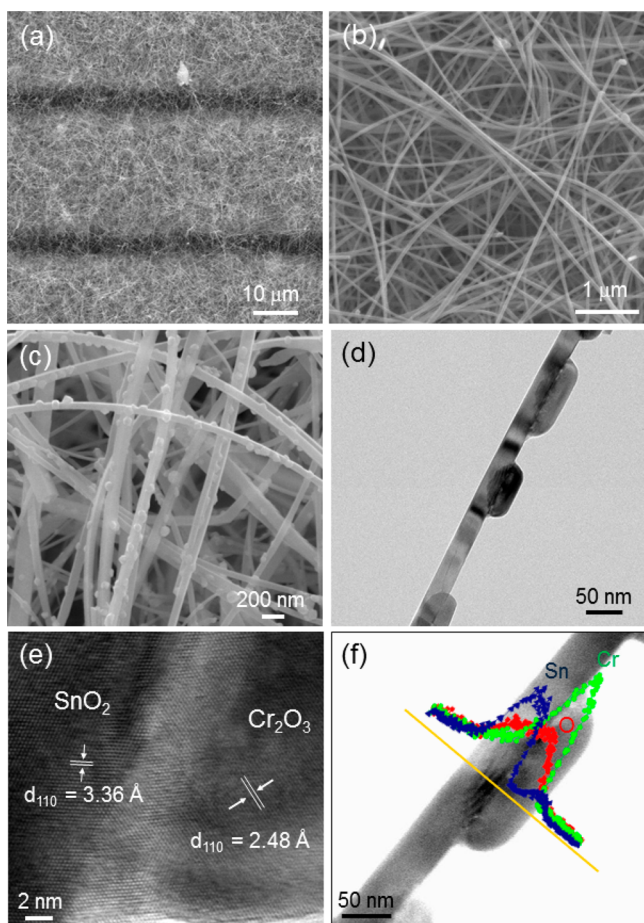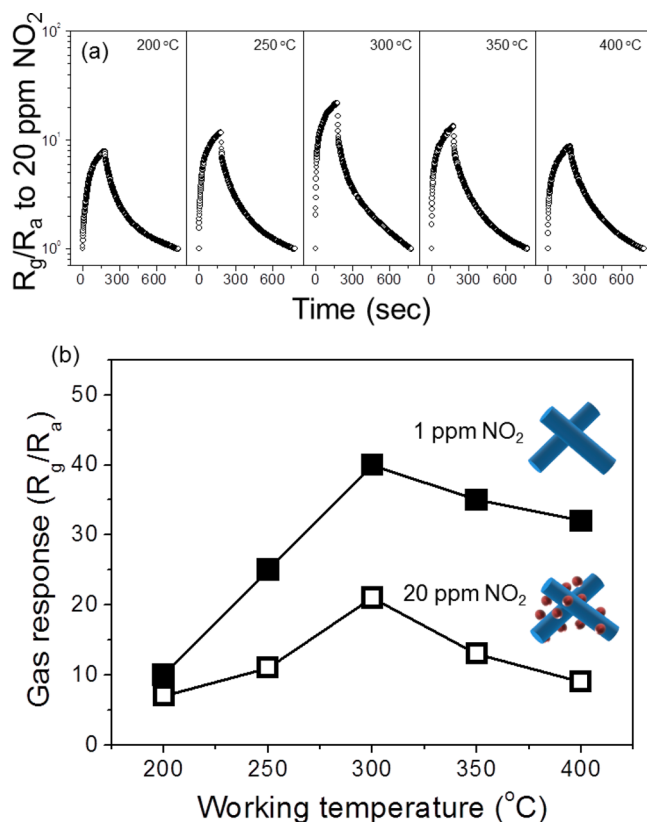
Figure 2. FE-SEM images of networks of *n*-SnO₂ NWs functionalized with *p*-Cr₂O₃ NPs: (a) plane view, (b) low magnification, and (c) high magnification. Typical TEM images: (d) low magnification, (e) high magnification, and (f) EDS elemental mapping profiles of Cr, Sn, and O in the region of a *p*-Cr₂O₃ NP.

Figure 3. (a) Response curves and (b) gas responses of *p*-Cr₂O₃ NPs-functionalized *n*-SnO₂ NWs, measured at various operating temperatures 200−400 °C in the presence of 20 ppm of NO₂. For comparison, gas responses of pristine *n*-SnO₂ NWs are also included.

lattice parameters $a = 4.9516$ Å and $c = 13.5987$ Å (JCPDS No. 84-1616). From the XRD results and the microstructure observations, it is reasonable to conclude that *p*-Cr₂O₃ NPs were successfully grown and attached on the SnO₂ NWs.

To determine the optimal operating temperature of the fabricated sensors, NO₂-sensing performances of the *p*-Cr₂O₃ NPs-functionalized *n*-SnO₂ NWs were investigated at various temperatures. Figure 3a shows the response and recovery curves obtained for 20 ppm of NO₂ over a temperature range 200−400 °C. For comparison, the results obtained for pristine SnO₂ NWs are also included in Figure 3b. The operating temperature has a big influence on the sensor's gas response. The best gas response was obtained at a temperature 300 °C. It should be mentioned here that the sensor in this study showed the largest response at 300 °C for all tested gases including H₂, CO, C₇H₈, and C₆H₆. On the basis of these results, all the other sensing measurements were performed at this temperature.

Sensing performances of the *p*-Cr₂O₃ NPs-functionalized *n*-SnO₂ NWs, with respect to various reducing gases, such as C₆H₆, C₇H₈, CO, and H₂, were investigated. The results of these experiments are summarized in Figure 4. Resistance values decreased immediately when the reducing gases were present and recovered their initial values completely when the reducing gases were removed and dry air was supplied. This dynamic resistance can be understood in terms of *n*-type

semiconducting metal oxide behavior. As shown in Figure 4a, the initial resistance (R_a) values of the *p*-Cr₂O₃ NPs-functionalized *n*-SnO₂ NWs sensor were 5 to 10 times larger than those of the pure SnO₂ NWs sensor. This indicates that the electron-depletion layer of the *n*-SnO₂ NWs is further expanded by the creation of Cr₂O₃−SnO₂ *p*−*n* heterojunctions. It is of note that the resistance modulation was more pronounced in the *p*-Cr₂O₃ NPs-functionalized *n*-SnO₂ NWs than in the pristine *n*-SnO₂ NWs. For comparison, Figure 4b summarizes the gas responses to 10 ppm of each reducing gas as bar graphs. It is clear that the attachment of *p*-Cr₂O₃ NPs greatly improves the reducing gas-sensing capabilities of *n*-SnO₂ NWs.

In addition, their sensing performances, with respect to various oxidizing gases, such as NO₂, O₂, and SO₂, were also investigated, and the results are shown in Figure 5. Resistances increased upon exposure to the oxidizing gases, which is typical behavior for *n*-type semiconductors. In sharp contrast to the case of reducing gases, resistance modulation was significantly reduced by the attachment of *p*-Cr₂O₃ NPs in the case of oxidizing gases. This is clearly shown in Figure 5b.

These phenomena are associated with the local suppression, in the radial direction, of the conduction channel of *n*-type NWs by functionalization with *p*-type NPs. This is shown schematically in Figure 6. For pristine SnO₂ NWs, as shown in Figure 6a, the conduction channel is established due to the adsorption of oxygen species in air, creating the electron-depletion layer near the NW surface. The width of the electron-depletion layer, which is equivalent to the Debye length of
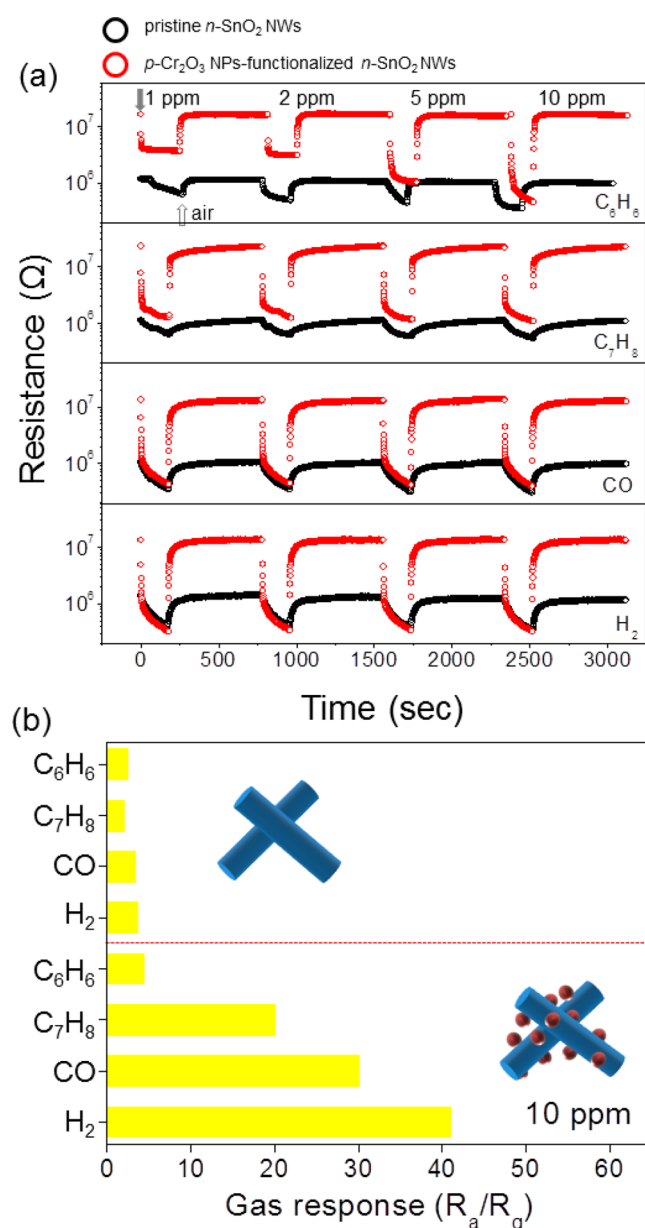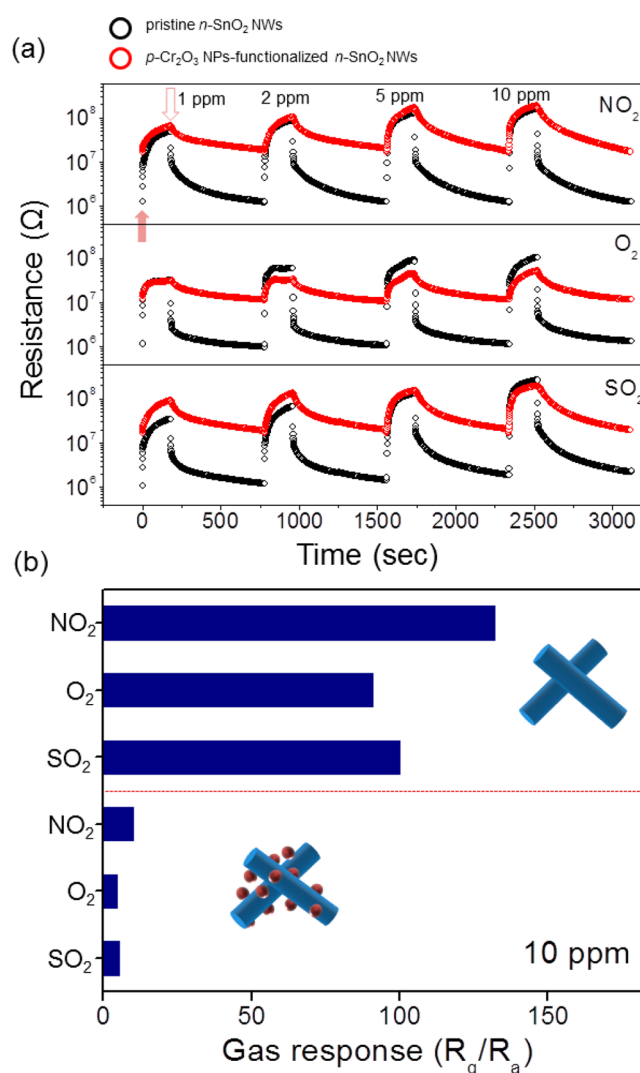
Figure 4. (a) Resistance curves obtained when p-Cr_2O_3 NPs-functionalized n-SnO_2 NWs were exposed to various reducing gases, such as H_2, CO, C_7H_8, and C_6H_6 at 300 °C. (b) Summary of gas responses to 10 ppm of each gas.

Figure 5. (a) Resistance curves obtained when p-Cr_2O_3 NPs-functionalized n-SnO_2 NWs were exposed to various oxidizing gases, such as SO_2, O_2, and NO_2 at 300 °C. (b) Summary of gas responses to 10 ppm of each gas.

pristine SnO_2 NWs, λ_d, caused by oxygen adsorption, and is defined as[32]

$$\lambda_d = \left[\frac{2\varepsilon SnO_2 \phi}{q^2 N_{SnO_2}} \right]^{1/2} \quad (1)$$

where ϕ is the height of the potential barrier established by the oxygen adsorption,[33] ε_{SnO_2} is the permittivity of SnO_2, N_{SnO_2} is the electron concentration in SnO_2, and q is the charge of an electron (=1.6×10^{-19} C). With the values $N_{SnO_2} \sim 3.6 \times 10^{18}$ cm^{-3} at room temperature, $\varepsilon_{SnO_2} \sim 1.61 \times 10^{-10}$ F·m^{-1}, and ϕ ~0.58 eV, the calculated width is approximately 18 nm. In this state, when an oxidizing gas is supplied, the electron-depletion layer expands further because oxidizing gas molecules extract conduction-band electrons. This results in the suppression of

the electrical transport channel and eventually leads to the increased resistance. On the other hand, when a reducing gas is supplied, the adsorbed oxygen species evaporates from the NW surface because the reducing gas molecules interact with them to form volatile molecules. This process causes captured electrons to return to the conduction band, resulting in shrinkage of the electron-depletion layer. This results in the decreased resistance when a reducing gas is supplied.

In contrast to the simple radial modulation of the electron-depletion layer operating in the pristine n-SnO_2 NWs, biased radial modulation occurs in p-Cr_2O_3 NPs-functionalized n-SnO_2 NWs as a result of carrier transfer between n-SnO_2 NWs and p-Cr_2O_3 NPs. As shown in Figure 6b, owing to the creation of p−n heterojunctions, electrons flow from n-SnO_2 NWs to p-Cr_2O_3 NPs and holes flow from p-Cr_2O_3 NPs to n-SnO_2 NWs until the build-up potential prevents such flow. This charge carrier transference makes electron−hole compensation possible in the vicinity of the p−n heterojunctions by reducing the hole concentration in the p-Cr_2O_3 NPs and electron concentration in the n-SnO_2 NWs. The corresponding band structure is also included in Figure 6b. To establish the band
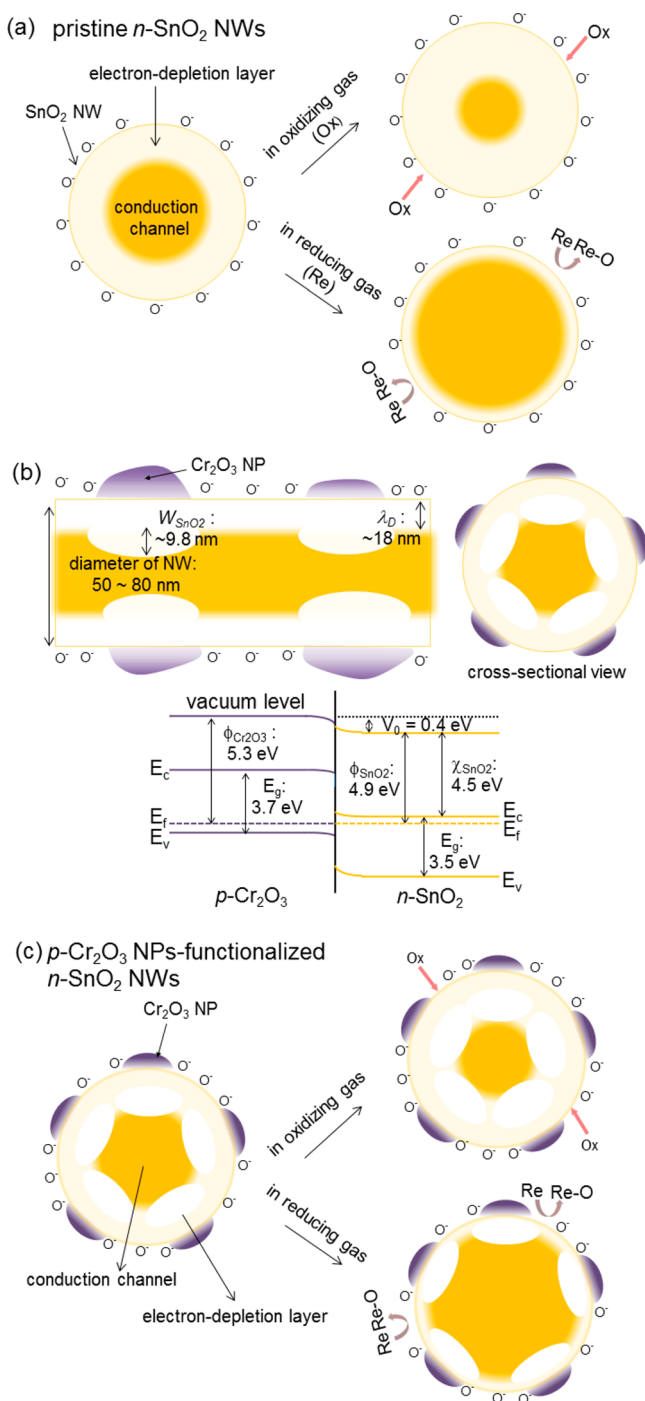
Figure 6. Schematics showing changes in the conduction channel of (a) pristine SnO_2 NWs, (b) the additional suppression of the conduction channel by electron transference and the related band structure at the $n-p$ heterojunctions, and (c) p-Cr_2O_3 NPs-functionalized n-SnO_2 NWs upon exposure to reducing or oxidizing gases.

structure, the electron affinities (χ), band gaps (E_g), and work functions (ϕ) of SnO_2 and Cr_2O_3 were required. E_{g,SnO_2} and E_{g,Cr_2O_3} values of 3.7 and 3.5 eV, and ϕ_{SnO_2} and $\phi_{Cr_2O_3}$ values of 4.9 and 5.3 eV were used, respectively, according to the previous findings.[34−37] The electron-depletion layer of n-SnO_2 NWs are further suppressed, in the radial direction, under p-Cr_2O_3 NPs, which significantly narrows their electrical

transport channel. The width of the space charge layers (W_{SnO_2} and $W_{Cr_2O_3}$) induced by the $p-n$ heterojunctions created between n-SnO_2 and p-Cr_2O_3 can be calculated using eqs 2 and 3 respectively,[38]

$$W_{SnO_2} = \left[\frac{2\varepsilon_{SnO_2}V_0}{q} \times \left\{ \frac{N_{Cr_2O_3}}{N_{SnO_2} \times (N_{SnO_2} + N_{Cr_2O_3})} \right\} \right]^{1/2}$$
(2)

$$W_{Cr_2O_3} = \left[\frac{2\varepsilon_{Cr_2O_3}V_0}{q} \times \left\{ \frac{N_{SnO_3}}{N_{Cr_2O_3} \times (N_{SnO_2} + N_{Cr_2O_3})} \right\} \right]^{1/2}$$
(3)

where ε_{SnO_2} and $\varepsilon_{Cr_2O_3}$ are 1.61×10^{-10} and 1.17×10^{-10} F·m^{-1}, respectively,[39,40] V_0 (=0.4 eV) is the contact potential difference between Cr_2O_3 and SnO_2, and $N_{Cr_2O_3}$ and N_{SnO_2} are the hole and electron concentrations, respectively ($N_{Cr_2O_3} = 2.8 \times 10^{18}$ and $N_{SnO_2} = 3.6 \times 10^{18}$ cm^{-3}).[41,42] The calculated W_{SnO_2} and $W_{Cr_2O_3}$ were ~9.8 nm and ~10.2 nm, respectively. As shown in Figure 6b, the widths of the space charge layers are superimposed onto the electron-depletion layer of the pristine SnO_2 NWs, resulting in additional suppression of the conduction channel as much as W_{SnO_2}. This explains why the attachment of p-Cr_2O_3 NPs significantly increases the resistance of n-SnO_2 NWs.

In the state of the additionally suppressed conduction channel, when reducing gases, such as CO, C_6H_6, C_7H_8, and H_2 are supplied, they induce the release of captured electrons and the shrinkage of the electron-depletion layer, which can become as thin as that of pristine n-SnO_2 NWs. This further modulates the resistivity of n-SnO_2 NWs, and is responsible for the improved sensing of reducing gases that is associated with the p-Cr_2O_3 NPs (see Figure 6c). It is interesting to note that the SnO_2 NWs showed a small variation in response for reducing gases, whereas p-Cr_2O_3 NPs-functionalized networked n-SnO_2 NWs showed the largest response to H_2. Ideally, the sensor should show a similar increase of response to all reducing gases. However, the large variation in response clearly indicates that the catalytic effect of p-Cr_2O_3 NPs greatly influences the chemisorption of reducing gas molecules. Particularly, Cr_2O_3 nanoparticles on SnO_2 nanowires catalytically facilitate both chemisorption and diffusion of hydrogen molecules while interacting with preadsorbed oxygen species and lattice O^{2-} ions at the Cr_2O_3 surface.[43−45] This chemical sensitization effect may additionally enhance the resistance modulation in the Cr_2O_3-functionalized SnO_2 nanowires for H_2 in comparison to other reducing gases. In contrast, when an oxidizing gas is supplied, the electron-depletion layer expands radially. However, different from the expansion behavior observed in pristine n-SnO_2 NWs, this expansion is marginal because the electron-depletion layer has already been expanded due to the $p-n$ heterojunction. This implies that the resistance modulation by oxidizing gases should be smaller than that of pristine n-SnO_2 NWs. The response and recovery times of the sensor in this work was 3−6 s toward all tested gases, which is shorter in comparison to the sensors prepared with Cr_2O_3 and other oxide materials reported.[46−51] However, the recovery time of the sensor in this work varies from 30 to 120 s. The long recovery time is quite common in chemoresistor-type semiconductor sensors due to slow desorption kinetic of gas

molecules. It is of note that the thickness of the Cr layer surely affects the final sensing properties because a thin layer produces a less populated or smaller-sized Cr_2O_3 NPs and a thick layer is likely to result in densely populated or bigger-sized Cr_2O_3 ones. The effect of amount of catalytic nanoparticles on sensing performance has been widely reported. According to the literature survey,[52−54] the volcano shape in the plot of concentration of catalytic particles versus sensor response is common. This indicates that an optimum amount of functionalized nanoparticles are essential to achieve the best sensing performances. The optimization of Cr_2O_3 NPs in terms of amount and size needs to be investigated in the future.

4. CONCLUSIONS

p-Cr_2O_3 NPs-functionalized networked n-SnO_2 NWs were investigated for their ability to sense various reducing and oxidizing gases. Networks of n-SnO_2 NWs were grown on SiO_2/Si substrates with patterned interdigital electrodes by the VLS method. Elongated p-Cr_2O_3 NPs functionalized the surface of the n-SnO_2 NWs. Functionalization with p-Cr_2O_3 NPs greatly improved the reducing gas-sensing properties of n-SnO_2 NWs but deteriorated their oxidizing-gas responses. These results are attributed to the electronic sensitization that occurred as a result of the local formation of $p−n$ heterojunctions, which leads to the additional expansion of the electron-depletion layer of n-SnO_2 NWs, being the source of the more pronounced resistance modulation of NWs. The results obtained from this study can be used as a primary design rule for obtaining n-type NWs that are sensitive to reducing gases.

■ ASSOCIATED CONTENT

Ⓢ Supporting Information

Additional information about the X-ray diffraction pattern of p-Cr_2O_3 NPs-functionalized networked n-SnO_2 NWs. This material is available free of charge via the Internet at http://pubs.acs.org.

■ AUTHOR INFORMATION

Corresponding Author
*S. S. Kim. E-mail: sangsub@inha.ac.kr.

Author Contributions
S.S.K. conceived the study, designed the experiments and prepared the paper. S.-W.C., A.K., and J.-H.K. performed the experiments. All authors have given approval to the final version of the paper.

Notes
The authors declare no competing financial interest.

■ ACKNOWLEDGMENTS

■ REFERENCES

(1) Kolmakov, A.; Moskovits, M. Chemical Sensing and Catalysis by One-Dimensional Metal-Oxide Nanostructure. *Annu. Rev. Mater. Res.* 2004, *34*, 151−180.

(2) Comini, E. Metal Oxide Nano-Crystals for Gas Sensing. *Anal. Chim. Acta* 2006, *568*, 28−40.

(3) Park, J. Y.; Choi, S.-W.; Jung, S.-H.; Kim, S. S. Synthesis of NiO Nanofibers and Their Gas Sensing Properties. *J. Nanosci. Nanotechnol.* 2012, *12*, 1288−1291.

(4) Liu, H.; Du, X.; Xing, X.; Wang, G.; Qiao, S. Z. Highly Ordered Mesoporous Cr_2O_3 Materials with Enhanced Performance for Gas Sensors and Litium Ion Batteries. *Chem. Commun.* 2012, *48*, 865−867.

(5) Sysoev, V. V.; Button, B. K.; Wepsiec, K.; Dmitriev, S.; Kolmakov, A. Toward the Nanoscopic "Electronic Nose": Hydrogen vs Carbon Monoxide Discrimination with an Array of Individual Metal Oxide Nano- and Mesowire Sensors. *Nano Lett.* 2006, *6*, 1584−1588.

(6) Mashock, M.; Yu, K.; Cui, S.; Mao, S.; Lu, G.; Chen, J. Modulation Gas Sensing Proeprties of CuO Nanowires through Creation of Discrete Nanosized P-N Junctions on Their Surfaces. *ACS Appl. Mater. Interfaces* 2012, *4*, 4192−4199.

(7) Choi, S.-W.; Katoch, A.; Zhang, J.; Kim, S. S. Electrospun Nanofibers of CuO-SnO_2 Nanocomposite as Semiconductor Gas Sensors for H_2S Detection. *Sens. Actuators, B* 2013, *176*, 585−591.

(8) Yoon, J.-W.; Kim, H.-J.; Kim, I.-D.; Lee, J.-H. Electronic Sensitization of the Response to C_2H_5OH of p-Type NiO Nanofibers by Fe Doping. *Nanotechnology* 2013, *24*, 444005.

(9) Choi, S.-W.; Jung, S.-H.; Kim, S. S. Functionalization of Selectively Grown Networked SnO_2 Nanowires with Pd Nanodots by γ-ray Radiolysis. *Nanotechnology* 2011, *22*, 225501.

(10) Sun, G.-J.; Choi, S.-W.; Katoch, A.; Wu, P.; Kim, S. S. Bi-Functional Mechanism of H_2S Detection Using CuO-SnO_2 Nanowires. *J. Mater. Chem. C* 2013, *1*, 5454−5462.

(11) Kolmakov, A.; Klenov, D. O.; Lilach, Y.; Stemmer, S.; Moskovits, M. Enhanced Gas Sensing by Individual SnO_2 Nanowires and Nanobelts Functionalized with Pd Catalyst Particles. *Nano Lett.* 2005, *5*, 667−673.

(12) Barth, S.; Jimenez.-Diaz, R.; Sama, J.; Prades, J. D.; Gracia, I.; Santander, J.; Cane, C.; Romano-Rodriguez, A. Localized Growth and in Situ Integration of Nanowires for Device Applications. *Chem. Commun.* 2012, *48*, 4734−4736.

(13) Xue, X.; Xing, L.; Chen, Y.; Shi, S.; Wang, Y.; Wang, T. Synthesis and H_2S Sensing Properties of CuO-SnO_2 Core/Shell PN-Junction Nanorods. *J. Phys. Chem. C* 2008, *112*, 12157−12160.

(14) Singh, B.; Ponzoni, A.; Gupta, R. K.; Lee, P. S.; Comini, E. Synthesis of In_2O_3-ZnO Core-Shell Nanowires and Their Application in Gas Sensing. *Sens. Actuators, B* 2011, *160*, 1346−1351.

(15) Le, D. T. T.; Trung, D. D.; Chinh, N. D.; Binh, B. T. T.; Hong, H. S.; Duy, N. V.; Hoa, N. D.; Hieu, N. V. Facile Synthesis of SnO_2-ZnO Core-Shell Nanowires for Enhanced Ethanol-Sensing Performance. *Curr. Appl. Phys.* 2013, *13*, 1637−1642.

(16) Choi, S.-W.; Park, J. Y.; Kim, S. S. Synthesis of SnO_2-ZnO Core-Shell Nanofibers via a Novel Two-Step Process and Their Gas Sensing Properties. *Nanotechnology* 2009, *20*, 465603.

(17) Park, J. Y.; Choi, S.-W.; Kim, S. S. A Synthesis and Sensing Application of Hollow ZnO Nanofibers with Uniform Wall Thickness Grown Using Polymer Templates. *Nanotechnology* 2010, *21*, 475601.

(18) Kim, H.-J.; Choi, K.-I.; Pan, A.; Kim, I.-D.; Kim, H.-R.; Kim, K.-M.; Na, C. W.; Cao, G.; Lee, J.-H. Template-Free Solvothermal Synthesis of Hollow Hematite Spheres and Their Application in Gas Sensors and Li-Ion Batteries. *J. Mater. Chem.* 2011, *21*, 6549−6555.

(19) Huang, H.; Gong, H.; Chow, C. L.; Guo, J.; White, T. J.; Tse, M. S.; Tan, O. K. Low-Temperature Growth of SnO_2 Nanorod Arrays and Tunable N-P-N Sensing Response of a ZnO-SnO_2 Heterojunction for Exclusive Hydrogen Sensors. *Adv. Funct. Mater.* 2011, *21*, 2680−2686.

(20) Khoang, N. D.; Trung, D. D.; Duy, N. V.; Hoa, N. D.; Hieu, N. V. Design of SnO_2/ZnO Hierarchical Nanostructures for Enhanced Ethanol Gas-Sensing Performance. *Sens. Actuators, B* 2012, *174*, 594−691.

(21) Wang, L.; Kang, Y.; Wang, Y.; Zhu, B.; Zhang, S.; Huang, W.; Wang, S. CuO Nanoparticle Decorated ZnO Nanorod Sensor for Low-Temperature H_2S Detection. *Mater. Sci. Eng., C* 2012, *32*, 2079−2085.

(22) Na, C. W.; Woo, H.-S; Lee, J.-H. Design of Highly Sensitive Volatile Organic Compound Sensors by Controlling NiO Loading on ZnO Nanowire Networks. *RSC Adv.* 2012, *2*, 414−417.

(23) Kuang, Q.; Lao, C.-S.; Li, Z.; Liu, Y.-Z.; Xie, Z.-X.; Zheng, L.-S.; Wang, Z. L. Enhancing the Photon- and Gas-Sensing Properties of a

17728

dx.doi.org/10.1021/am504164j | *ACS Appl. Mater. Interfaces* 2014, *6*, 17723−17729

Single SnO_2 Nanowire based Nanodevice by Nanoparticle Surface Functioinalizatioin. *J. Phys. Chem. C* **2008**, *112*, 11539−11544.

(24) Zeng, W.; Liua, T.; Wang, Z. Enhanced Gas Sensing Properties by SnO_2 Nanosphere Functionalized TiO_2 Nanobelts. *J. Mater. Chem.* **2012**, *22*, 3544−3548.

(25) Na, C. W.; Park, S.-Y.; Chung, J.-H.; Lee, J.-H. Transformation of ZnO Nanobelts into Single-Crystalline Mn_3O_4 Nanowires. *ACS Appl. Mater. Interfaces* **2012**, *4*, 6565−6572.

(26) Mathur, S.; Barth, Sven. Molecule-based Chemical Vapor Growth of Aligned SnO_2 Nanowires and Branched SnO_2/V_2O_5 Heterostructure. *Small* **2007**, *3*, 2070−2075.

(27) Choi, S.-W.; Katoch, A.; Sun, G.-J.; Wu, P.; Kim, S. S. NO_2-Sensing Performance of SnO_2 Microrods by Functionalizaiton of Ag Nanoparticles. *J. Mater. Chem. C* **2013**, *1*, 2834−2841.

(28) Hoffmann, M. W. G.; Prades, J. D.; Mayrhofer, L.; Hernandez-Ramirez, F.; Järvi, T. T.; Moseler, M.; Waag, A.; Shen, H. Highly Selective SAM-Nanowire Hybrid NO_2 Sensor: Insight into Charge Transfer Dynamics and Alignment of Frontier Molecular Orbitals. *Adv. Funct. Mater.* **2014**, *24*, 595−602.

(29) Katoch, A.; Choi, S.-W.; Sun, G.-J.; Kim, S. S. An Approach to Detecting a Reducing Gas by Radial Modulation of Electron-Depleted Shells in Core-Shell Nanofibers. *J. Mater. Chem. A* **2013**, *1*, 13588−13596.

(30) Park, J. Y.; Choi, S.-W.; Kim, S. S. Junction-Tuned SnO_2 Nanowires and Their Sensing Properties. *J. Phys. Chem. C* **2011**, *115*, 12774−12781.

(31) Woo, H.-S.; Na, C. W.; Kim, I.-D.; Lee, J.-H. Highly Sensitive and Selective Trimethylamine Sensor Using One-Dimensional ZnO-Cr_2O_3 Hetero-Nanostructures. *Nanotechnology* **2012**, *23*, 245501.

(32) Vanheusden, K.; Warren, W. L.; Seager, C. H.; Tallant, D. R.; Voigt, J. A. Mechanisms behind Green Photoluminescence in ZnO Phosphor Powder. *J. Appl. Phys.* **1996**, *79*, 7983.

(33) Liao, Z. M.; Liu, K. J.; Zhang, J. M.; Xu, J.; Yu, D. P. Effect of Surface States on Electron Transport in Individual ZnO Nanowires. *Phys. Lett. A* **2007**, *367*, 207−210.

(34) Luo, S.; Fan, J.; Liu, W.; Zhang, M.; Song, Z.; Lin, C.; Wu, X.; Chu, P. K. Synthesis and Low-Temperature Photoluminescence Properties of SnO_2 Nanowires and Nanobelts. *Nanotechnology* **2006**, *17*, 1695−1699.

(35) Könenkamp, R.; Word, R. C.; Godinez, M. Electoluminescence in Nanoporous TiO_2 Solid-State Heterojunctions. *Nanotechnology* **2006**, *17*, 1858−1861.

(36) Marchetti, L.; Perrin, S.; Wouters, Y.; Martin, F.; Pijolat, M. Photoelectrochemical Study of Nickel Base Alloys Oxide Films Formed at High Temperature and High Pressure Water. *Electrochim. Acta* **2010**, *55*, 5384−5392.

(37) Greiner, M. T.; Helander, M. G.; Tang, W.-M.; Wang, Z.-B.; Qiu, J.; Lu, Z.-H. Universal Energy-Level Alignment of Molecules on Metal Oxides. *Nat. Mater.* **2012**, *11*, 76−81.

(38) Streetman, B. G.; Banerjee, S. K. *Solid State Electronic Devices*, 6th ed.; Pearson Education Inc.: Upper Saddle River, NJ, 2005.

(39) Borges, P. D.; Scolfaro, L. M. R.; Alves, H. W. L.; Da Silva, E. F., Jr.; Assali, L. V. C. DFT Study of the Electronic, Vibrational, and Optical Properties of SnO_2. *Theor. Chem. Acc.* **2010**, *126*, 39−44.

(40) Fang, P. H.; Brower, W. S. Dielectric Constant of Cr_2O_3 Crystals. *Phys. Rev.* **1963**, *129*, 1561.

(41) Qin, P.; Fang, G.; Sun, N.; Fan, X.; Zheng, Q.; Chen, F.; Wan, J.; Zhao, X. Organic Solar Cells with p-Type Amorphous Chromic Oxide Thin Film as Hole-Transporting Layer. *Thin Solid Films* **2011**, *519*, 4334−4341.

(42) Cheng, Y.; Yang, R.; Zheng, J.-P.; Wang, Z. L.; Xiong, P. Characterizing Individual SnO_2 Nanobelt Field-Effect Transistors and Their Intrinsic Responses to Hydrogen and Ambient Gases. *Mater. Chem. Phys.* **2012**, *137*, 372−380.

(43) Ostrovskii, V. E.; Kadyshevich, E. A.; Gostev, B. V.; Lapidus, A. L. An Adsorption and Calorimetric Study of the Interaction of Hydrogen with Chromium Oxide. *Russ. J. Phys. Chem.* **2008**, *82*, 1626−1632.

(44) Ostrovskii, V. E.; Kadyshevich, E. A.; Gostev, B. V.; Lapidus, A. L. Chemisorption of O_2, H_2, and H_2O Vapor at Cr_2O_3: Molar Heat Effects, Rates, and Mechanisms of Chemisorption. *Russ. J. Phys. Chem.* **2009**, *83*, 1946−1953.

(45) Chen, C. F.; Yu, H. B.; Zheng, S. Q. First-Principles Study of Hydrogen Diffusion Mechanism in Cr_2O_3. *Sci. China: Technol. Sci.* **2011**, *54*, 88−94.

(46) Patil, D. R.; Patil, L. A.; Patil, P. P. Cr_2O_3-Activated ZnO Thick Film Resistors for Ammonia Gas Sensing Operable at Room Temperature. *Sens. Actuators, B* **2007**, *126*, 368−374.

(47) Suryawanshi, D. N.; Patil, D. R.; Patil, L. A. Fe_2O_3-Activated Cr_2O_3 Thick Films as Temperature Dependent Gas Sensors. *Sens. Actuators, B* **2008**, *134*, 579−584.

(48) Patil, D. R.; Patil, L. Cr_2O_3-Modified ZnO Thick Film Resistors as LPG Sensors. *Talanta* **2009**, *77*, 1409−1414.

(49) Balouria, V.; Kumara, A.; Singh, A.; Samanta, S.; Debnath, A. K.; Mahajan, A.; Bedi, R. K.; Aswal, D. K.; Gupta, S. K.; Yakhmi, J. V. Temperature Dependent H_2S and Cl_2 Sensing Selectivity of Cr_2O_3 Thin Films. *Sens. Actuators, B* **2011**, *157*, 466−472.

(50) Gao, P.; Ji, H.; Zhou, Y.; Li, X. Selective Acetone Gas Sensors using Porous WO_3−Cr_2O_3 Thin Films Prepared by Sol−Gel Method. *Thin Solid Films* **2012**, *520*, 3100−3106.

(51) Kwak, C.-H.; Woo, H.-S.; Lee, J.-H. Selective Trimethylamine Sensors Using Cr_2O_3-Decorated SnO_2 Nanowires. *Sens. Actuators, B* **2014**, *204*, 231−238.

(52) Korotcenkov, G.; Cho, B. K.; Gulina, L.; Tolstoy, V. SnO_2 Thin Films Modified by the SnO_2−Au Nanocomposites: Response to Reducing Gases. *Sens. Actuators, B* **2009**, *141*, 610−616.

(53) Hwang, I.-S.; Choi, J.-K.; Woo, H.-S.; Kim, S.-J.; Jung, S.-Y.; Seong, T.-Y.; Kim, I.-D.; Lee, J.-H. Facile Control of C_2H_5OH Sensing Characteristics by Decorating Discrete Ag Nanoclusters on SnO_2 Nanowire Networks. *ACS Appl. Mater. Interfaces* **2011**, *3*, 3140−3145.

(54) Wongrat, E.; Hongsith, N.; Wongratanaphisan, D.; Gardchareon, A.; Choopun, S. Control of Depletion Layer Width via Amount of AuNPs for Sensor Response Enhancement in ZnO Nanostructure Sensor. *Sens. Actuators, B* **2012**, *171−172*, 230−237.